

A COMPARISON OF THE DISPERSION AND DISSIPATION ERRORS OF GAUSS AND GAUSS–LOBATTO DISCONTINUOUS GALERKIN SPECTRAL ELEMENT METHODS*

GREGOR GASSNER[†] AND DAVID A. KOPRIVA[‡]

Abstract. We examine the dispersion and dissipation properties of the Gauss and Gauss–Lobatto discontinuous Galerkin spectral element methods (DGSEMs), for linear wave propagation problems. We show that the inherent underintegration in the Gauss–Lobatto variant can be interpreted as a modal filtering of the highest polynomial mode. This in turn has a drastic impact on the dispersion and dissipation relations of the Gauss–Lobatto DGSEM compared to the Gauss variant. We show that the Gauss DGSEM is typically more accurate than the Gauss–Lobatto variant, needing fewer points per wavelength for a given accuracy while on the other hand being more restricted in the explicit time step choice. We show that the spectra of the DGSEM operators depend on the boundary conditions applied and that the ratio of the time step restrictions of the two schemes depends on the choice of boundary conditions.

Key words. discontinuous Galerkin spectral element method, Gauss Legendre, Gauss–Lobatto Legendre, dissipation, dispersion

AMS subject classification. 65G99

DOI. 10.1137/100807211

1. Introduction. This paper compares the wave propagation properties of two implementations of the discontinuous Galerkin collocation spectral element method. The discontinuous Galerkin spectral element method (DGSEM) is used in a wide range of applications such as compressible flows [4], [5], [20], electromagnetics and optics [17], [18], [8], [7], aeroacoustics [21], [24], [26], [6], meteorology [11], [12], [22], and geophysics [9], [10]. The dispersion and dissipation properties of the discontinuous Galerkin scheme have been investigated and documented by Hu, Hussaini, and Rasetarinera [14], Stanescu, Kopriva, and Hussaini [25], Sherwin [23] and Ainsworth [2]. In those works, the authors used exact evaluation of the volume and surface integrals to define the semidiscrete operators used for the analysis. In [1], Ainsworth and Wajid did a comparison of the effects of full and underintegration for continuous spectral element methods for second order problems.

In this work, the influence of two integration rules for the discontinuous spectral element method applied to first order problems is investigated. In the collocation-type implementation of the DGSEM scheme, there are two common sets of integration/interpolation points. The Gauss–Lobatto Legendre points include the end points of the interval and have integration precision $2N - 1$ when choosing $N + 1$ points, whereas the Gauss Legendre points have integration precision $2N + 1$ as they do not include the boundary points. For linear wave propagation as used in this work for the analysis of the wave propagation properties, the integration precision of the Gauss DGSEM variant is sufficient for evaluating all occurring integrals exactly. Thus

*Submitted to the journal’s Methods and Algorithms for Scientific Computing section September 1, 2010; accepted for publication (in revised form) August 4, 2011; published electronically October 18, 2011.

<http://www.siam.org/journals/sisc/33-5/80721.html>

[†]Institute for Aerodynamics and Gasdynamics, Universität Stuttgart, 70550 Stuttgart, Germany (gassner@uni-stuttgart.de).

[‡]Department of Mathematics, The Florida State University, Tallahassee, FL 32312 (kopriva@math.fsu.edu). This author’s research was supported in part by NSF grant DMS-0810925.

for this variant of the scheme, the results documented in [14] and [25] are expected. However, in the Gauss–Lobatto variant, the integration precision is insufficient for the exact evaluation of the local mass matrix, and as a result, an additional integration error often termed as *mass lumping* is introduced. With Gauss–Lobatto, therefore, we expect the dispersion and dissipation properties to differ. In this paper the effect of Gauss–Lobatto underintegration on the wave propagation properties is investigated and compared to the properties of the Gauss DGSEM variant.

2. DGSEM approximation of conservation laws. In this section, we describe the discontinuous Galerkin spectral element method for one-dimensional scalar hyperbolic equations of the form

$$(2.1) \quad u_t + f_x(u) = 0,$$

with suitable boundary and initial conditions. We start by subdividing the computational space in nonoverlapping intervals $I_k := [x_k; x_{k+1}]$. For each grid cell, the equations are transformed to the master element $E = [1; -1]$ via the linear transform $x(\xi)$. The mapped equation for the grid cell k reads as

$$(2.2) \quad \frac{\Delta x_k}{2} u_t + f_\xi(u) = 0.$$

We get the weak formulation by multiplying by a test function $\ell_i(\xi)$, integrating over the master element

$$(2.3) \quad \int_E \left(\frac{\Delta x_k}{2} u_t + f_\xi(u) \right) \ell_i d\xi = 0,$$

and using integration by parts to separate boundary and volume contributions

$$(2.4) \quad \int_E \frac{\Delta x_k}{2} u_t \ell_i d\xi + f(u) \ell_i|_{\partial E} - \int_E f(u) (\ell_i)_\xi d\xi = 0.$$

For the approximation of the solution and the flux function, we choose polynomials with degree N for each grid cell, where we denote the associated space of polynomials with degree less than or equal to N as \mathbb{P}^N . A basis for \mathbb{P}^N is the set of Lagrange interpolating polynomials, $\ell_j(\xi)$, $j = 0, \dots, N$,

$$(2.5) \quad \ell_j(\xi) = \prod_{\substack{i=0 \\ i \neq j}}^N \frac{(\xi - \xi_i)}{(\xi_j - \xi_i)}.$$

With this set of basis functions, the approximate solution is

$$(2.6) \quad u(\xi, t)|_{I_k} \approx u_k(\xi, t) = \sum_{j=0}^N u_j^k(t) \ell_j(\xi),$$

where $u_j^k(t) := u_k(\xi_j, t)$. We note that generally the approximate solution is discontinuous across grid cell interfaces. The flux is approximated by interpolation using the same basis functions

$$(2.7) \quad f(u)|_{I_k} \approx f_k(\xi) = \sum_{j=0}^N f_j^k \ell_j(\xi),$$

where $f_j^k := f(u_j^k)$. Due to the discontinuous approximation space, the flux function in the boundary contribution is not uniquely defined and is thus replaced by a suitable numerical flux function (see, e.g., [28]),

$$(2.8) \quad f|_{\partial E} \approx f^* = f^*(u^-, u^+),$$

where u^\pm denotes the value from the left and right grid cell at the grid cell interface. With this approximation, the integrand in the first volume integral in the discontinuous Galerkin formulation (2.4) is a polynomial in \mathbb{P}^{2N} and the integrand in the second volume integral is a polynomial in \mathbb{P}^{2N-1} .

We proceed by approximating the volume integrals with integration rules. To get nodal and orthogonal basis functions, we choose the interpolation points in (2.5) to be the same as the integration points, i.e., we choose either a Gauss or Gauss–Lobatto rule with precision $2N + \delta$, where we have $\delta = 1$ for Gauss and $\delta = -1$ for Gauss–Lobatto:

$$(2.9) \quad \int_E u(\xi) v(\xi) d\xi = (u, v) \approx (u, v)_N := \sum_{n=0}^N u(\xi_n) v(\xi_n) \omega_n,$$

where $\{\xi_n\}_{n=0}^N$ and ω_n , $n = 0, \dots, N$ are the integration nodes and weights, respectively. When using Gauss integration, all integrals are evaluated exactly whereas Gauss–Lobatto integration introduces an additional integration error for the first volume integral, which we will analyze later in detail.

Inserting these approximations into the discontinuous Galerkin formulation (2.4), we end up with the following DGSEM:

$$(2.10) \quad \frac{du_i^k}{dt} = -\frac{2}{\Delta x_k} \left\{ f^*|_{\xi=1} \frac{\ell_i(1)}{\omega_i} - f^*|_{\xi=-1} \frac{\ell_i(-1)}{\omega_i} + \sum_{j=0}^N f_j^k \widehat{D}_{ij} \right\},$$

with

$$(2.11) \quad \underline{\underline{\widehat{D}}} := -\underline{\underline{\widetilde{M}}}^{-1} \underline{\underline{D}}^T \underline{\underline{\widetilde{M}}}.$$

Here $\underline{\underline{D}}$ denotes the differentiation matrix $D_{ij} := (\ell_j)_\xi(\xi_i)$, and $\underline{\underline{\widetilde{M}}}$ is the discrete local mass matrix with components

$$(2.12) \quad \widetilde{M}_{ij} := (\ell_j, \ell_i)_N = \delta_{ij} \omega_i.$$

3. The influence of Gauss–Lobatto integration. In this section, we investigate the influence of the insufficient integration precision of the Gauss–Lobatto rule. As noted in the last section, Gauss–Lobatto integration introduces an additional integration error when approximating the first volume integral, i.e., when computing the mass matrix

$$(3.1) \quad M_{ij} = \int_E \ell_j \ell_i d\xi, \quad \text{or} \quad \underline{\underline{M}} = \int_E \underline{\underline{\ell}} \underline{\underline{\ell}}^T d\xi,$$

where $\underline{\underline{\ell}} = (\ell_0, \dots, \ell_N)^T$. We note that if we would compute the mass matrix exactly, the resulting scheme would be equal to the nodal discontinuous Galerkin (DG) scheme introduced by Hesthaven and Warburton; see, e.g. [13]. To show the effect of the Gauss–Lobatto integration, we introduce the normalized Legendre basis functions

$\phi_j(\xi)$, which are hierarchically sorted in the sense that the index j indicates the maximum polynomial degree of the basis function. Interpolating the Legendre basis function with the Lagrange basis functions (2.5) gives us the transformation

$$(3.2) \quad \underline{\varphi}(\xi) = \underline{\underline{V}}^{-T} \underline{\ell}(\xi),$$

where $\underline{\underline{V}}$ denotes the Vandermonde matrix with entries

$$(3.3) \quad V_{ij} = \varphi_j(\xi_i),$$

where ξ_i are the Gauss-Lobatto nodes. Using this transformation, the mass matrix (3.1) can be reformulated as

$$(3.4) \quad \begin{aligned} \underline{\underline{M}} &= \int_{-1}^1 \underline{\ell}(\xi) \underline{\ell}^T(\xi) d\xi \\ &= \underline{\underline{V}}^{-T} \int_{-1}^1 \underline{\varphi}(\xi) \underline{\varphi}^T(\xi) d\xi \underline{\underline{V}}^{-1} \\ &=: \underline{\underline{V}}^{-T} \widehat{\underline{\underline{M}}} \underline{\underline{V}}^{-1}, \end{aligned}$$

where $\widehat{\underline{\underline{M}}}$ is the modal mass matrix. Note that for an exact evaluation of the inner product, e.g., when using Gauss integration, the modal mass matrix is

$$(3.5) \quad \widehat{M}_{ij} := \int_{-1}^1 \varphi_j(\xi) \varphi_i(\xi) d\xi =: (\varphi_j, \varphi_i) = \delta_{ij}.$$

If we approximate the inner product with Gauss-Lobatto integration, we get

$$(3.6) \quad \widehat{\widehat{M}}_{ij} := (\varphi_j, \varphi_i)_N^{GL} = \begin{cases} \delta_{ij} & \text{for } i + j \neq 2N, \\ (\varphi_N, \varphi_N)_N^{GL} & \text{for } i = j = N. \end{cases}$$

The normalized Legendre basis with degree N is

$$(3.7) \quad \varphi_N(\xi) = \sqrt{\frac{2N+1}{2}} \phi_N(\xi),$$

where $\phi_N(\xi)$ denotes the N th standard Legendre function. Using Gauss-Lobatto integration with $N+1$ points, the discrete inner product of the N th Legendre basis function reduces to

$$(3.8) \quad (\phi_N, \phi_N)_N^{GL} = \frac{2}{N}$$

(see, e.g., [15]). Thus the last entry of the discrete local mass matrix (3.6) is

$$(3.9) \quad (\varphi_N, \varphi_N)_N^{GL} = \frac{2N+1}{N} \longrightarrow 2 \quad \text{for } N \mapsto \infty.$$

If we take a closer look at the effect of the insufficient integration of the mass matrix, we recognize that we need the inverse of the mass matrix to compute the time derivative of the nodal degrees of freedom $\frac{du_i^k}{dt}$. We thus get the relation

$$(3.10) \quad \widetilde{\underline{\underline{M}}}^{-1} = \widetilde{\underline{\underline{M}}}^{-1} \underline{\underline{M}} \underline{\underline{M}}^{-1} =: \underline{\underline{F}} \underline{\underline{M}}^{-1},$$

where the new matrix $\underline{\underline{F}}$ contains the effect of the insufficient Gauss–Lobatto precision compared to an exact evaluation of the mass matrix. This matrix can be simplified by using (3.4) and (3.5):

$$\begin{aligned}
 \underline{\underline{F}} &= \widetilde{\underline{\underline{M}}}^{-1} \underline{\underline{M}} \\
 &= \left(\underline{\underline{V}}^{-T} \widehat{\underline{\underline{M}}} \underline{\underline{V}}^{-1} \right)^{-1} \left(\underline{\underline{V}}^{-T} \widehat{\underline{\underline{M}}} \underline{\underline{V}}^{-1} \right) \\
 &= \left(\underline{\underline{V}} \widehat{\underline{\underline{M}}}^{-1} \underline{\underline{V}}^T \right) \left(\underline{\underline{V}}^{-T} \widehat{\underline{\underline{M}}} \underline{\underline{V}}^{-1} \right) \\
 &= \underline{\underline{V}} \widehat{\underline{\underline{M}}}^{-1} \underline{\underline{V}}^{-1}.
 \end{aligned}
 \tag{3.11}$$

The structure of the matrix $\underline{\underline{F}}$ reveals that the effect of the Gauss–Lobatto integration is equal to a modal filter, with the associated modal filter coefficients given by

$$\sigma_j := \widehat{\underline{\underline{M}}}^{-1}_{jj} = \begin{cases} 1 & \text{for } j < N, \\ \frac{N}{2N+1} & \text{for } j = N. \end{cases}
 \tag{3.12}$$

This shows that all modes of the time derivative are unaffected except for the highest mode, which is multiplied by a factor of $\frac{N}{2N+1} < 1$. If we thus compare the Gauss–Lobatto DGSEM to the nodal DG method [13] with Gauss–Lobatto nodes in one dimension, the effect of insufficient integration is that the highest mode gets damped. To investigate the effect of this modal filter on the wave propagation properties of the methods, we focus next on the analysis of the dispersion errors of both schemes.

4. Dispersion analysis. The method used in this section to investigate the dispersion properties is similar to the one presented by Hu, Hussaini, and Rasetarinera [14]. We focus on the scalar one-dimensional periodic linear transport problem

$$\begin{aligned}
 u_t + a u_x &= 0, \\
 u(x, t) &= e^{i(kx - \omega t)},
 \end{aligned}
 \tag{4.1}$$

where $a = \text{const} > 0$ is the transport velocity and $\omega = ka$. For a given grid cell $I_l := [x_l; x_{l+1}]$, the discontinuous Galerkin spectral element scheme (2.10) in matrix-vector notation is

$$\frac{\Delta x_l}{2} \widetilde{\underline{\underline{M}}} \frac{\partial \underline{\underline{u}}^l}{\partial t} + a \underline{\underline{S}} \underline{\underline{u}}^{l-1} + a \underline{\underline{E}} \underline{\underline{u}}^l = \underline{\underline{0}},
 \tag{4.2}$$

where $\underline{\underline{u}}^l := (u_0^l(t), \dots, u_N^l(t))^T$, and the matrices are

$$\begin{aligned}
 \widetilde{\underline{\underline{M}}}_{ij} &= \delta_{ij} \omega_l, \\
 \underline{\underline{S}}_{ij} &= -\ell_i(-1)\ell_j(1), \\
 \underline{\underline{E}}_{ij} &= \ell_i(1)\ell_j(1) - D_{ji}\omega_j.
 \end{aligned}
 \tag{4.3}$$

We note that for the approximation of the surface flux we choose a purely upwind flux.

We assume that the mesh is uniform $\Delta x_l = \Delta x$ and $x_l = l \Delta x$ and seek solutions of the form

$$\underline{\underline{u}}^l = \widehat{\underline{\underline{u}}} e^{i(l\Delta x - \omega t)},
 \tag{4.4}$$

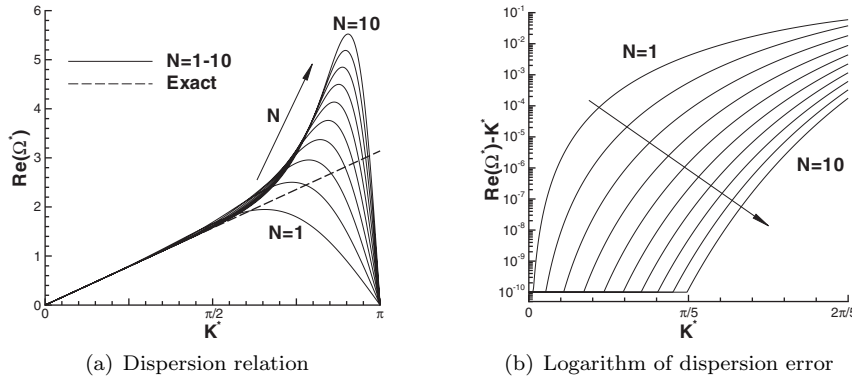


FIG. 4.1. Real part of the physical mode for the Gauss DGSEM scheme with $N = 1$ up to $N = 10$. In the logarithmic plot, the error is cut off at 10^{-10} to avoid numerical noise.

where $\hat{\underline{u}}$ is a complex vector of dimension $N + 1$. Inserting this into (4.2), we get the following expression:

$$(4.5) \quad \left(\frac{-i\omega\Delta x}{2} \underline{\widetilde{M}} + a e^{-ik\Delta x} \underline{\underline{S}} + a \underline{\underline{E}} \right) \hat{\underline{u}} = \underline{0}.$$

Substituting $\Omega := \frac{\omega\Delta x}{a}$ and $K := k\Delta x$, we get the following algebraic eigenvalue problem:

$$(4.6) \quad \underbrace{\frac{2}{i} \underline{\widetilde{M}}^{-1} (e^{-iK} \underline{\underline{S}} + \underline{\underline{E}})}_{=: \underline{\underline{A}}} \hat{\underline{u}} = \Omega \hat{\underline{u}},$$

where $\underline{\underline{A}} \in \mathbb{C}^{(N+1) \times (N+1)}$ is the matrix, $\hat{\underline{u}} \in \mathbb{C}^{N+1}$ the eigenvector, and $\Omega \in \mathbb{C}$ the eigenvalue. We note that for a given K , we get $N+1$ eigenvalues $\Omega(K)_i$ (i.e., numerical modes) for each grid cell. Similar to the work of Hu, Hussaini, and Rasetarinera [14], we define the *physical mode* as one with the frequency that approximates the exact dispersion relation for a range of wave numbers. The others are the *parasite modes* associated with the numerical schemes. It is easy to extract the physical mode by using the exact relation

$$(4.7) \quad \begin{aligned} \operatorname{Re}(\Omega_{ex}(K)) &= K, \\ \operatorname{Im}(\Omega_{ex}(K)) &= 0, \end{aligned}$$

where $\operatorname{Re}()$ denotes the real part and $\operatorname{Im}()$ the imaginary part of the complex number. We can now investigate the influence of the approximation by computing the eigenvalue corresponding to the physical mode for different values of K and compare it to the exact relation (4.7).

The plots in Figure 4.1 show the dispersion relation for the scheme with Gauss points. The eigenvalues have been normalized by the number of grid points in each grid cell for each polynomial degree

$$(4.8) \quad K^* = \frac{K}{N+1} \quad \text{and} \quad \Omega^* = \frac{\Omega}{N+1}.$$

We note that for this linear example, the Gauss scheme and the nodal DG scheme [13] are exact, in the sense that all integrals are evaluated exactly. Figure 4.1(a) shows

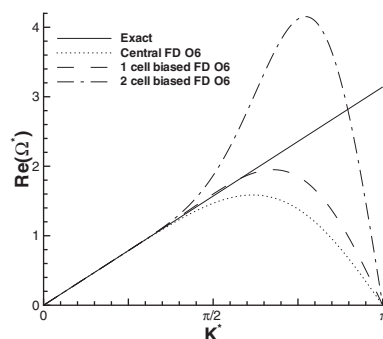


FIG. 4.2. Real part of the physical mode for 6th order central, 1-cell biased, and 2-cell biased explicit FD schemes. The more biased the scheme, the higher the overshoots.

the DG dispersion relation, with the typical large overshoots with respect to the exact relation for large values of K^* . This is a common effect for one-sided approximations, as can be seen in Figure 4.2, where the dispersion relation of a 6th order central finite difference (FD) scheme, a one cell biased 6th order FD scheme, and a two cell biased 6th order FD scheme are shown. Appendix A contains the detailed dispersion relations for these schemes. We note that for FD approximations, $K^* = K$ and $\Omega^* = \Omega$. The plot clearly shows that the maximum of $Re(\Omega^*)$ increases for the two cell biased FD scheme, similar to the DG dispersion relation.

The bias in DG schemes can directly be attributed to the derivative matrix $\underline{\underline{D}}$. To show this, it is possible to reformulate the discontinuous Galerkin scheme (2.4), where an additional (back) integration by parts is used to get the so-called *strong formulation* of the scheme

$$(4.9) \quad \int_E \frac{\Delta x_k}{2} u_t \ell_i d\xi + (f^*(u^\pm) - f^-) \ell_i|_{\partial E} + \int_E f_\xi(u) \ell_i d\xi = 0,$$

where f^- is the value of the interpolated flux function from inside the grid cell. It was shown by the authors in [16] that for both variants of the DGSEM scheme, Gauss and Gauss-Lobatto, the schemes from either one integration by parts or two integration by parts are equivalent, as long as global flux interpolations are used. The strong formulation (4.9) allows an interpretation of the method as a spectral penalty scheme [13], where the surface contribution is for stabilization only. The main part of the scheme is therefore the volume term, which is

$$(4.10) \quad \int_E f_\xi(u) \underline{\underline{\ell}} d\xi \approx \underline{\underline{D}} f,$$

when inserting polynomial approximations. For nodal approximations, each row of the differentiation matrix $\underline{\underline{D}}$ contains the coefficients of an associated FD formula. To see this, we choose the illustrative case of Gauss-Lobatto points with $N = 2$. This case is special, as it gives a regular node distribution inside the grid cell

$$(4.11) \quad \xi_0 = -1 \quad \text{and} \quad \xi_1 = 0 \quad \text{and} \quad \xi_2 = 1.$$

If we compute the coefficients of the derivative matrix $\underline{\underline{D}}$, we get

$$(4.12) \quad \underline{\underline{D}} = \frac{1}{2} \begin{pmatrix} 3 & -4 & 1 \\ 1 & 0 & -1 \\ -1 & 4 & -3 \end{pmatrix},$$

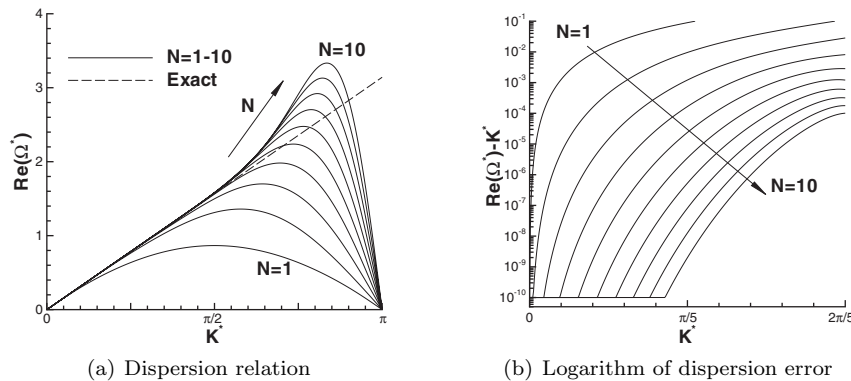


FIG. 4.3. Real part of the physical mode for the Gauss-Lobatto DGSEM scheme with $N = 1$ up to $N = 10$. In the logarithmic plot, the error is cut off at 10^{-10} to avoid numerical noise.

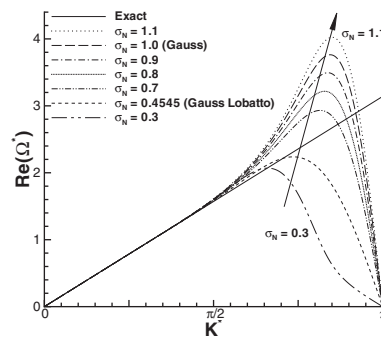


FIG. 4.4. Real part of the physical mode for DGSEM with $N = 5$ and different modal filter coefficients σ_N .

where the first row has the coefficients of the left biased FD scheme and the second row the classic central FD scheme; the last row corresponds to the right biased FD scheme. The bias in the DG scheme is even amplified for higher order polynomial approximations. Although no direct comparison to existing FD formulae can be made due to the nonuniform node distribution, the bias still stems from the fact that one-sided interpolations are used to construct the rows of the derivative matrix \underline{D} .

The same analysis for the DGSEM with Gauss-Lobatto nodes reveals a significantly different behavior between the two schemes. The results of this analysis are presented in Figure 4.3, where again the dispersion relation and the logarithm of the dispersion error are plotted. The most noticeable impact of the modal filter due to the Gauss-Lobatto underintegration is the reduced maxima of the dispersion relation curves and thus a drastic reduction of the overshoots. Up to about degree $N = 5$ the whole dispersion relation is located on the bottom side of the exact relation, common to most central discretizations.

We note that we can transform the dispersion relation of the Gauss scheme into the dispersion relation of the Gauss-Lobatto scheme by applying the modal filter (3.12) and vice versa. The effects of different modal filter coefficients are plotted in Figure 4.4. We choose here the Gauss DGSEM scheme with $N = 5$ and apply a modal filter where all filter coefficients are equal to 1 except for the last one σ_N . If we choose

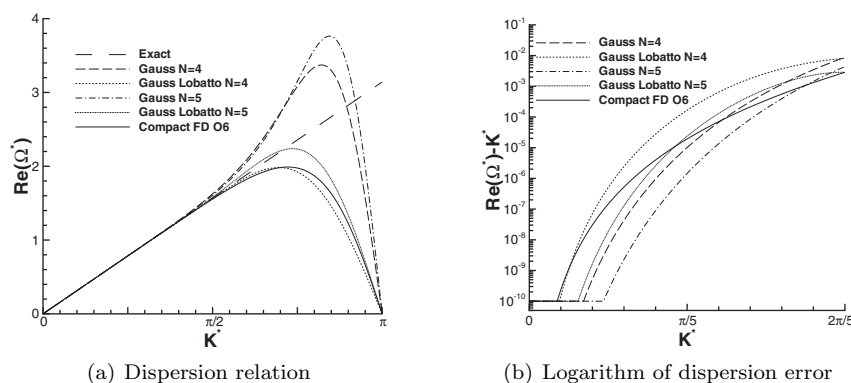


FIG. 4.5. Comparison of the dispersion relation for Gauss and Gauss-Lobatto DGSEM with $N = 4$, $N = 5$, and a 6th order compact FD scheme [3]; see Appendix A. In the logarithmic plot, the error is cut off at 10^{-10} to avoid numerical noise.

$\sigma_N = 1$, we don't modify the scheme at all. If we choose $\sigma_N = \frac{N}{2N+1} = 0.4545$, we get the Gauss-Lobatto scheme. The plots clearly show that the maximum value of the dispersion relation decreases with an increased filter strength.

If we compare the logarithmic plots of the dispersion error in Figures 4.1(b) and 4.3(b), we see a considerable advantage of the Gauss DGSEM scheme. For a detailed comparison, Figure 4.5 shows the plots for $N = 4$ and $N = 5$. Furthermore, the dispersion relation of a 6th order compact FD scheme [3] is included; see Appendix A for more details.

To quantify the accuracy, we define the dispersion error as

$$(4.13) \quad \delta := |Re(\Omega(K)) - K|,$$

and seek for a given accuracy δ the corresponding minimum wavenumber K_{\min} , to compute resolution in points per wavelength

$$(4.14) \quad PPW_{\min}(N, \delta) := \frac{2\pi(N+1)}{K_{\min}(\delta)}.$$

The results for different accuracies and different polynomial degrees N are given in Tables 4.1 and 4.2, where the corresponding points per wavelength for the 6th order compact FD scheme are listed for comparison. We replaced the minimum search by a discrete process with 1000 sample points. For low polynomial degrees N , the results clearly show that Gauss is far more accurate than the Gauss-Lobatto variant. Furthermore, the higher the accuracy requirement δ , the better Gauss is in comparison to Gauss-Lobatto. The results also indicate that the advantage of the Gauss scheme decreases the higher the polynomial degree N becomes. For $N = 10$ and low dispersion errors, Gauss-Lobatto is even slightly more accurate than Gauss.

The impact of the modal filter shown in Figure 4.4 suggests that it may be possible to tune the modal filter coefficients σ_N to optimize the dispersion relation. For a given accuracy δ , it is possible to find the optimal modal coefficient σ_N^{opt} , in the sense that the points per wavelength requirement is minimized. We have listed results for such an optimization in Tables 4.3 and 4.4 for an approximation with polynomial degree $N = 5$ and $N = 10$, respectively. Again, the minimum search is replaced by a discrete process, where 200 sample points are chosen to find the optimum in the interval

TABLE 4.1

$PPW_{\min}(N, \delta)$ for the Gauss DGSEM and the 6th order compact FD for a given dispersion error δ .

$\delta \backslash N$	1	2	3	4	5	6	7	8	9	10	FD
0.01	9.61	7.60	6.53	5.91	5.49	5.20	4.98	4.80	4.67	4.55	4.22
0.001	15.98	10.86	8.65	7.48	6.75	6.24	5.88	5.60	5.37	5.19	5.76
0.0001	25.62	15.25	11.35	9.38	8.22	7.43	6.87	6.45	6.13	5.86	7.93
0.00001	41.63	21.26	14.80	11.68	9.89	8.76	7.96	7.37	6.94	6.57	10.92

TABLE 4.2

$PPW_{\min}(N, \delta)$ for the Gauss-Lobatto DGSEM and the 6th order compact FD for a given dispersion error δ .

$\delta \backslash N$	1	2	3	4	5	6	7	8	9	10	FD
0.01	31.22	12.97	8.80	7.01	5.96	4.45	4.47	4.44	4.40	4.35	4.22
0.001	68.90	21.48	12.97	9.79	8.12	7.11	6.42	5.93	5.52	5.14	5.76
0.0001	153.69	34.45	18.50	13.06	10.41	8.88	7.87	7.16	6.64	6.22	7.93
0.00001	333.00	55.50	25.95	17.08	13.06	10.80	9.43	8.43	7.71	7.19	10.92

TABLE 4.3

$PPW_{\min}(\delta)$ for the DGSEM with $N = 5$ and different pointwise optimized modal coefficients σ_N^{opt} and the DRP-like optimized variant with $\sigma_N^{DRP}(K_{\max}^* = 1.1) = 0.8127$. For comparison, the Gauss ($\sigma_N = 1$) DGSEM, the Gauss-Lobatto ($\sigma_N = 0.4545$) DGSEM with $N = 5$, and the 6th order compact FD scheme results are listed as well. The bold numbers denote the optimal points per wavelength for the corresponding accuracy for the DGSEM.

$\delta \backslash \sigma_N^{opt}$	0.5920	0.7749	0.8593	0.9085	DRP	Gauss	Gauss-Lobatto	FD
0.01	4.42	4.93	5.18	5.23	5.05	5.49	5.96	4.22
0.001	7.66	5.43	6.02	6.32	5.69	6.24	8.12	5.76
0.0001	9.84	8.84	6.55	7.27	8.50	8.22	10.41	7.93
0.00001	12.41	11.29	10.46	7.90	10.98	9.89	13.06	10.92

TABLE 4.4

$PPW_{\min}(\delta)$ for the DGSEM with $N = 10$ and different optimized modal coefficients σ_N^{opt} and the DRP-like optimized variant with $\sigma_N^{DRP}(K_{\max}^* = 1.1) = 0.8127$. For comparison, the Gauss ($\sigma_N = 1$) DGSEM, the Gauss-Lobatto ($\sigma_N = 0.4762$) DGSEM with $N = 10$, and the 6th order compact FD scheme results are listed as well. The bold numbers denote the optimal points per wavelength for the corresponding accuracy for the DGSEM.

$\delta \backslash \sigma_N^{opt}$	0.5286	0.5322	0.7221	0.7995	DRP	Gauss	Gauss-Lobatto	FD
0.01	4.32	4.32	4.37	4.43	4.44	4.55	4.35	4.22
0.001	5.00	4.58	4.80	4.93	4.96	5.05	5.14	5.76
0.0001	6.17	6.15	5.06	5.37	5.43	5.86	6.22	7.93
0.00001	7.11	7.09	6.68	5.64	5.74	6.57	7.19	10.92

$\sigma \in [0.3; 1]$. The values of the optimized modal filter coefficients are sorted, in the sense that the first column and the associated value σ_N^{opt} corresponds to the optimal value for the lowest accuracy requirement $\delta = 0.01$, and the last column corresponds to the optimal scheme when using the highest accuracy requirement $\delta = 0.00001$.

The results reveal that it is indeed possible to optimize the DGSEM with a modal filter with respect to the dispersion relation. We also investigated the choice $\sigma_N < 0.3$ and $\sigma_N > 1$ and $\sigma_{N-1} \neq 1$, without getting any significant improvements.

Further results of the optimization process indicate that for higher accuracy requirements the optimal modal coefficient σ_N^{opt} slowly converges to 1, i.e., to the Gauss

DGSEM. The convergence of the optimization process towards the Gauss DGSEM is slower with respect to the accuracy requirements for large N . For instance we get $\sigma_N^{opt}(\delta = 10^{-11}) = 0.9930$ for $N = 5$ and $\sigma_N^{opt}(\delta = 10^{-11}) = 0.9543$ for $N = 10$. In contrast to this high accuracy requirement case, it seems that in the case of better resolved approximations (larger N for a given accuracy δ or lower accuracy requirements δ for a given polynomial degree N) the optimization process tends towards an increased damping coefficient σ_N , similar to the Gauss–Lobatto scheme.

Another possibility for optimizing the dispersion relation of the scheme is to use not only a pointwise value, but an integral measure. Tam and Shen [27] used the L_2 norm of the dispersion error up to a value $K_{\max}^* = 1.1$, which means that they optimized their so-called dispersion relation preserving (DRP) scheme for a points per wavelength value of $ppw_{\min}^{DRP} = 2\pi/1.1 \approx 5.7$ and higher values. The results for this DRP-like optimization are listed in Tables 4.3 and 4.4.

Carrying out this DRP-like optimization process for different DGSEM approximations yields an astounding result. The modal damping coefficients converge towards a fixed value for approximations with increased polynomial degree N . For instance we get $\sigma_N^{DRP}(K_{\max}^* = 1.1) = 0.8127$ for approximations with polynomial degree $N \geq 5$. We get the value $\sigma_N^{DRP}(K_{\max}^* = 1.2) = 0.7612$ for polynomial approximations with degree $N \geq 7$. Furthermore, the value of the optimized modal coefficient seems to converge itself with the value of K_{\max}^* . We get for instance $\sigma_N^{DRP}(K_{\max}^* = 1.0) = 0.8525$ for polynomial approximations with degree $N \geq 5$ and $\sigma_N^{DRP}(K_{\max}^* = 0.5) = 0.9672$ for polynomial approximations with degree $N \geq 2$. The convergence of the DRP-like optimization indicates that the value of the modal coefficients converge towards one, i.e., the Gauss DGSEM, for small values of K_{\max}^* , i.e., the well-resolved case. This fits very well within the observation of the pointwise optimized procedure, that in the well-resolved case the optimization process tends towards the Gauss DGSEM scheme. It is highly debatable if this one-dimensional linear analysis carries over to the more general multidimensional discretizations with curved/unstructured grids. The applicability of the optimized dispersion DGSEM to the general case is an ongoing research topic and will be investigated in future work. We will also see in section 6 that the modal damping filter increases the overall dissipation of the scheme and thus alters the resolution requirements.

5. Analysis of the eigenvalue spectrum and the time step restriction.

The advantageous dispersion accuracy of the Gauss DGSEM compared to the Gauss–Lobatto scheme comes at a price, namely, the large overshoots of the dispersion relation. The maximum of the dispersion curve is strongly related to the maximal allowable time step in the sense that the higher the overshoot the more severe the time step restriction. To quantify this effect we focus in this section on the time step restriction and the eigenvalue spectra of the schemes.

The time step restriction in an explicit method of lines approach depends on the spectrum of the spatial operator and the stability region of the time integration scheme. We investigate the time step restriction for DGSEM discretizations of linear wave propagation problems as derived in section 4. For the time integration, we combine these schemes with a Taylor time discretization method, yielding a Taylor DG approximation [19].

5.1. Periodic boundary conditions. In this section, the stability of the Taylor DGSEM for a one-dimensional scalar linear advection problem with periodic boundary conditions is investigated. We therefore compute the eigenspectrum of the operator matrix. The individual eigenvalues are used to determine the stable time step of the

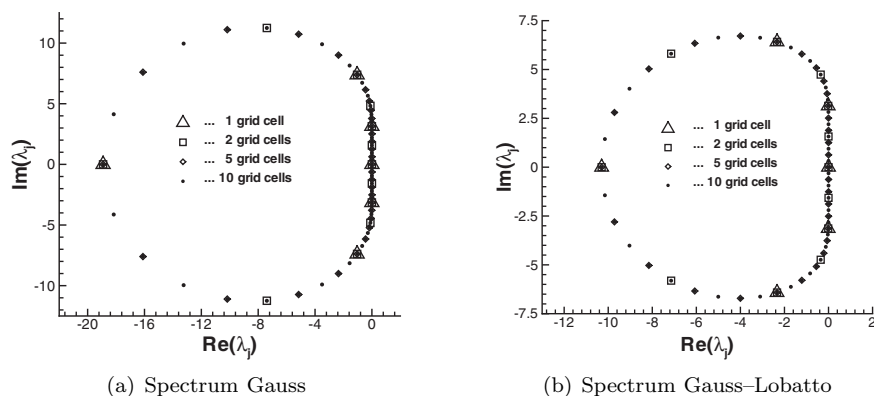


FIG. 5.1. Plot of the spectra for Gauss and Gauss-Lobatto DGSEM with $N = 5$, periodic boundary conditions, and different numbers of grid cells.

TABLE 5.1

Normalized stability numbers CFL^* for Gauss DGSEM with periodic boundary conditions and different combinations of polynomial degree N and Taylor time integration with order M . The bold numbers indicate when $M = N + 1$, where the order of the time approximation is equal to the approximation order in space.

$N \backslash M$	2	3	4	5	6	7	8	9	10	11
1	0.67	0.82	0.93	1.07	1.18	1.32	1.44	1.57	1.69	1.82
2	0.37	0.63	0.71	0.81	0.90	1.00	1.09	1.19	1.28	1.38
3	0.22	0.52	0.58	0.67	0.74	0.83	0.90	0.98	1.06	1.14
4	0.17	0.45	0.50	0.58	0.64	0.71	0.77	0.84	0.91	0.98
5	0.14	0.40	0.44	0.51	0.56	0.63	0.68	0.75	0.80	0.86
6	0.12	0.36	0.40	0.46	0.5070	0.56	0.62	0.67	0.72	0.78
7	0.11	0.33	0.36	0.42	0.4620	0.51	0.56	0.61	0.66	0.71
8	0.10	0.30	0.33	0.39	0.4259	0.47	0.52	0.56	0.61	0.65
9	0.09	0.28	0.31	0.36	0.3955	0.44	0.48	0.52	0.56	0.61
10	0.09	0.26	0.29	0.33	0.3695	0.41	0.45	0.49	0.53	0.57

discretization. In a first step, we investigate the influence of the number of grid cells (elements) on the spectrum of the spatial operator. Figure 5.1 shows the spectrum of the Gauss DGSEM for an approximation with $N = 5$ and different grid cell numbers. We can see that the influence on the eigenvalue extrema of the number of grid cells is rather small, as long as the grid cell number provides the leading eigenvalue with $Im(\lambda_j) = 0$. The plots furthermore reveal that the stiffness of the two approximations is quite different and that this should have a drastic impact on the time step stability of the two schemes.

With the eigenvalues of the spatial operators, it is now possible to find the maximum stable time step. For the following investigation, we choose the setup with 10 grid cells. The following Tables 5.1 and 5.2 contain the stability numbers (CFL^*) for different combinations of polynomial degree N and time order M . The stability numbers are normalized with respect to the degrees of freedom (number of grid points) per grid cell

$$(5.1) \quad CFL^* := \frac{\Delta t(N+1)}{\Delta x|a|},$$

where Δx is the DGSEM grid cell (element) width, $|a|$ is the transport velocity (see

TABLE 5.2

Normalized stability numbers CFL^* for Gauss–Lobatto DGSEM with periodic boundary conditions and different combinations of polynomial degree N and Taylor time integration with order M . The bold numbers indicate the case when $M = N + 1$, where the order of the time approximation is equal to the approximation order in space.

$N \backslash M$	2	3	4	5	6	7	8	9	10	11
1	2.00	2.14	2.47	2.92	3.20	3.56	3.92	4.24	4.60	4.94
2	0.53	1.35	1.54	1.78	1.97	2.19	2.39	2.60	2.81	3.017
3	0.30	1.02	1.15	1.33	1.47	1.64	1.79	1.95	2.10	2.26
4	0.20	0.84	0.95	1.06	1.21	1.34	1.46	1.60	1.72	1.85
5	0.16	0.72	0.81	0.84	1.03	1.15	1.26	1.37	1.48	1.59
6	0.14	0.64	0.72	0.71	0.91	1.017	1.11	1.21	1.30	1.40
7	0.12	0.58	0.65	0.62	0.82	0.92	1.00	1.08	1.17	1.26
8	0.11	0.53	0.59	0.57	0.75	0.84	0.92	0.99	1.07	1.15
9	0.10	0.49	0.54	0.52	0.69	0.77	0.84	0.92	0.99	1.06
10	0.10	0.45	0.51	0.49	0.64	0.71	0.78	0.85	0.92	0.99

TABLE 5.3

Normalized stability numbers CFL^* for optimized $N = 5$ DGSEM with periodic boundary conditions for different time orders M . The DRP-like optimized scheme has a modal damping coefficient $\sigma_N^{DRP}(K_{\max}^* = 1.1) = 0.8127$. The bold numbers indicate the case $M = N + 1 = 6$, where the order of the time approximation is equal to the approximation order in space. For comparison, the corresponding numbers of an $N = 5$ Gauss and Gauss–Lobatto DGSEM are listed, respectively.

$\sigma_N^{opt} \backslash M$	2	3	4	5	6	7	8	9	10	11
0.5920	0.15	0.58	0.65	0.75	0.83	0.92	1.00	1.09	1.18	1.27
0.7749	0.14	0.48	0.53	0.61	0.68	0.75	0.82	0.89	0.96	1.04
0.8593	0.14	0.44	0.49	0.57	0.63	0.70	0.76	0.83	0.89	0.96
0.9085	0.14	0.42	0.47	0.55	0.60	0.67	0.73	0.80	0.86	0.92
DRP	0.14	0.46	0.51	0.60	0.65	0.73	0.79	0.86	0.93	1.00
Gauss	0.14	0.40	0.44	0.51	0.56	0.63	0.68	0.75	0.80	0.86
Gauss–Lobatto	0.16	0.72	0.81	0.84	1.03	1.15	1.26	1.37	1.48	1.59

(4.1)), and $N + 1$ is the number of grid points per grid cell for a given polynomial degree N . We note that the typical normalization for DG schemes is not the number of grid points $N + 1$, but $2N + 1$. This follows from the fact that when choosing the time order equal to the spatial order $M = N + 1$, the CFL numbers with respect to $2N + 1$ are equal to one, pointing towards a natural normalization for the DG scheme. However, from the user point of view it is much more helpful to know the stability numbers with respect to the grid nodes $N + 1$.

Comparing the time steps of the Gauss and Gauss–Lobatto scheme to each other, we see that we get a factor of about two higher for the Gauss–Lobatto scheme. If we look at Table 5.2, we see that for $M = N + 1$, the normalized stability numbers are equal to about one, whereas the normalized stability numbers for the Gauss DGSEM are about $\frac{1}{2}$. The only exception is the case $N = 1$ for Gauss–Lobatto and $M = 2$, where the spectrum of the spatial operator is identical to the stability curve of the time integrator, thus resulting in a nonnormalized stability number of $CFL = 1$. We have also included the stability numbers for the optimized DGSEM schemes in Tables 5.3 and 5.4. We can see that the damping parameter has a direct influence on the stability number, which varies between the values of the Gauss and Gauss–Lobatto DGSEM.

TABLE 5.4

Normalized stability numbers CFL^* for optimized $N = 10$ DGSEM with periodic boundary conditions for different time orders M . The DRP-like optimized scheme has a modal damping coefficient $\sigma_N^{DRP}(K_{\max}^* = 1.1) = 0.8127$. The bold numbers indicate the case $M = N + 1 = 11$, where the order of the time approximation is equal to the approximation order in space. For comparison, the corresponding numbers of an $N = 10$ Gauss and Gauss-Lobatto DGSEM are listed, respectively.

$\sigma_N^{opt} \backslash M$	2	3	4	5	6	7	8	9	10	11
0.5286	0.10	0.41	0.45	0.48	0.58	0.65	0.70	0.77	0.83	0.89
0.5322	0.10	0.41	0.45	0.48	0.58	0.64	0.70	0.76	0.82	0.88
0.7221	0.09	0.32	0.36	0.41	0.45	0.51	0.55	0.60	0.65	0.70
0.7995	0.09	0.30	0.33	0.38	0.42	0.47	0.52	0.56	0.61	0.65
DRP	0.09	0.30	0.33	0.38	0.42	0.47	0.51	0.56	0.60	0.65
Gauss	0.09	0.26	0.29	0.33	0.37	0.41	0.45	0.49	0.53	0.57
Gauss-Lobatto	0.10	0.45	0.51	0.49	0.64	0.72	0.78	0.85	0.92	0.99

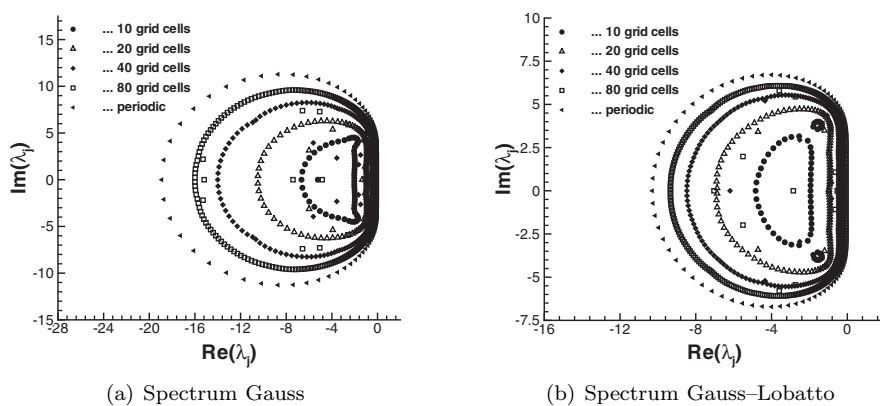


FIG. 5.2. Plot of the spectra for Gauss and Gauss-Lobatto DGSEM with $N = 5$, exact boundary conditions, and different numbers of grid cells. For comparison, the periodic spectrum with 10 grid cells is plotted as well.

5.2. Exact boundary conditions. Up to now, we have considered only periodic boundary conditions. We will see in this section that the boundary conditions have a drastic impact on the stability numbers of the schemes. To show this, the stability of the Taylor DGSEM for a one-dimensional scalar linear advection problem with upwind specified (Dirichlet) boundary conditions is investigated. We compute again the eigenspectrum of the operator matrix to determine the stable time step of the discretization. As before, in a first step, we investigate the influence of the number of grid cells on the spectrum of the spatial operator. As an example, Figure 5.2 shows the resulting spectrum of the Gauss DGSEM for an approximation with $N = 5$ and different grid cell numbers.

We can see now that the number of grid cells has a major impact on the spectrum of the operator. For reference, the spectrum for periodic boundary conditions is plotted as well. For a large number of grid cells, the spectra converge to the periodic spectra, revealing that the periodic case is in some sense the worst case scenario; i.e., we get larger time steps when considering exact boundary conditions. Stability numbers for approximations with $N = 5$ and $M = N + 1 = 6$ for different number of grid cells are listed in Table 5.5.

It is also worth noting that the influence of the different boundary conditions is much more pronounced for the Gauss DGSEM compared to the Gauss-Lobatto

TABLE 5.5

Normalized stability numbers CFL^* for $N = 5$ DGSEM with exact boundary conditions for time order $M = N + 1 = 6$ and different numbers of grid cells. For comparison, the corresponding numbers in the case of periodic boundary conditions are listed. The last row contains the ratios of the stability numbers.

# grid cells	10	20	40	80	Periodic
Gauss	1.5998	1.0162	0.7609	0.6664	0.5633
Gauss–Lobatto	2.2017	1.5408	1.2580	1.1407	1.0346
Ratio	1.3763	1.5163	1.6532	1.7118	1.8366

DGSEM; i.e., the stiffness of the Gauss DGSEM increases more with N compared to the Gauss–Lobatto DGSEM. This, in fact, has direct influence on the ratios of the maximum stable time steps. Looking at Table 5.5, the ratio of the stability numbers is about ~ 1.38 for 10 grid cells, whereas for 80 grid cells the value is about ~ 1.72 , approaching the ratio of the periodic case. It is highly debatable if the reduced stiffness of the exact boundary condition case can be used to increase the time step in real life computations, as it is very difficult to judge the actual stability number. If one does not want to manually choose the time step for each computation, it seems to be more reasonable to use the stability numbers of the periodic case to get a safe automatic estimation of the maximum allowable time step.

6. Dissipation analysis. Considering the effect of modal filtering, it is clear that this has a drastic impact on the dissipation behavior of the scheme as well. We will see in this section that the modal filtering typically decreases the dissipation accuracy as well and that the resolution requirements for a given dissipation accuracy are slightly more severe than the points per wavelength needed for the same dispersion accuracy.

For the dissipation analysis, we use the same method described in section 4 for the dispersion analysis. This time, the imaginary part of the eigenvalue is compared to the exact relation, not the real part (see (4.7)). We investigate the influence of the numerical approximation by comparing the eigenvalue corresponding to the physical mode for different values of K to the exact relation for diffusion

$$(6.1) \quad \operatorname{Im}(\Omega_{ex}(K)) = 0.$$

Figures 6.1 and 6.2 show the dissipation relation and the logarithm of the dissipation error. Again, the eigenvalues have been normalized by the number of grid points in each grid cell for each polynomial degree

$$(6.2) \quad K^* = \frac{K}{N+1} \quad \text{and} \quad \Omega^* = \frac{\Omega}{N+1}.$$

We note that we did not include the compact FD scheme for comparison, as its dissipation error is zero. The additional stability and dissipation needed for the approximation of nonlinear equations within those schemes is provided by filtering techniques that are not well suited for comparison since the effect depends on the implementation, the time integration method, and the time step.

Comparing the dissipation relations of the Gauss and the Gauss–Lobatto DGSEM reveals that again the Gauss scheme is the more accurate one. For a detailed quantification, we look again at the points per wavelength for a given dissipation error,

$$(6.3) \quad \delta := |\operatorname{Im}(\Omega(K))|.$$

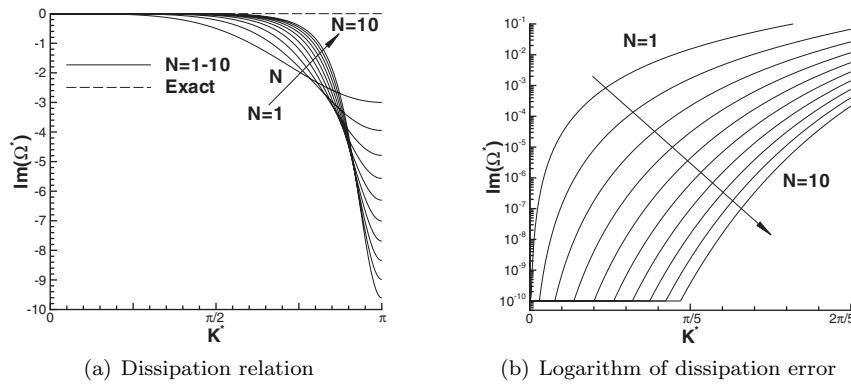


FIG. 6.1. Imaginary part of the physical mode for the Gauss DGSEM scheme with $N = 1$ up to $N = 10$. In the logarithmic plot, the error is cut off at 10^{-10} to avoid numerical noise.

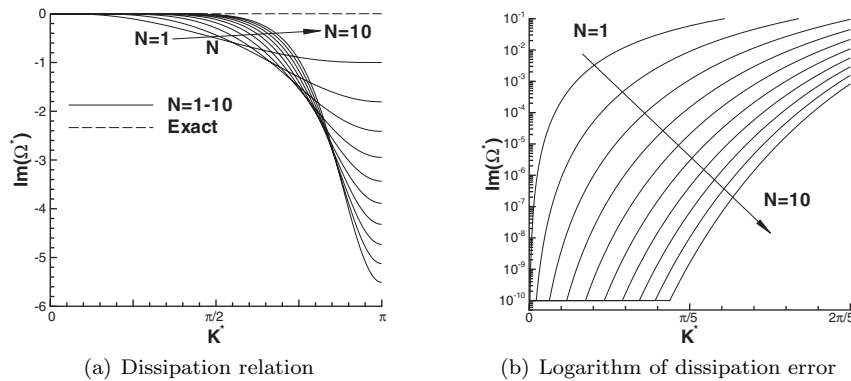


FIG. 6.2. Imaginary part of the physical mode for the Gauss-Lobatto DGSEM scheme with $N = 1$ up to $N = 10$. In the logarithmic plot, the error is cut off at 10^{-10} to avoid numerical noise.

TABLE 6.1
 $PPW_{\min}(N, \delta)$ for the Gauss DGSEM for a given dissipation error δ .

$\delta \backslash N$	1	2	3	4	5	6	7	8	9	10
0.01	13.41	8.84	7.14	6.24	5.71	5.33	5.06	4.86	4.70	4.56
0.001	24.37	13.32	9.84	8.16	7.16	6.53	6.07	5.74	5.47	5.27
0.0001	43.43	19.78	13.32	10.46	8.88	7.87	7.19	6.68	6.30	6.00
0.00001	76.85	29.38	18.00	13.32	10.92	9.42	8.43	7.74	7.21	6.80

The results are listed in Tables 6.1 and 6.2. We can see that the dissipation advantage of the Gauss scheme, like the dispersion accuracy, decreases with increasing polynomial degree N . Evaluating the resolution requirements of the Gauss scheme, we get the well-known result that the dispersion error is dominated by the dissipation errors and that the accuracy requirements for the dissipation are more severe; see Hu, Hussaini, and Rasetarinera [14]. However, with the Gauss-Lobatto scheme, we can see that it is either the dispersion error that dominates for low order polynomial discretizations or that both errors require about the same resolution.

If we use the modal filtering mechanism again to search for the optimum scheme with respect to the dissipation error, it is clear that this optimization process always

TABLE 6.2
 $PPW_{\min}(N, \delta)$ for the Gauss–Lobatto DGSEM for a given dissipation error δ .

$\delta \backslash N$	1	2	3	4	5	6	7	8	9	10
0.01	21.96	12.11	8.96	7.48	6.64	6.07	5.68	5.39	5.16	4.98
0.001	41.62	18.16	12.26	9.70	8.29	7.37	6.77	6.32	5.98	5.71
0.0001	76.85	27.00	16.65	12.41	10.19	8.88	7.99	7.35	6.87	6.49
0.00001	133.20	39.96	22.20	15.73	12.49	10.57	9.34	8.47	7.80	7.32

TABLE 6.3
 $PPW_{\min}(\delta)$ for the DGSEM with $N = 5$ and different pointwise optimized modal coefficients σ_N^{opt} and the DRP-like optimized variant with $\sigma_N^{DRP}(K_{\max}^* = 1.1) = 0.8127$. For comparison, the Gauss ($\sigma_N = 1$) DGSEM and the Gauss–Lobatto ($\sigma_N = 0.4545$) DGSEM with $N = 5$ are listed as well. Note that the optimization is with respect to dispersion; see Table 4.3 for comparison.

$\delta \backslash \sigma_N^{opt}$	0.5920	0.7749	0.8593	0.9085	DRP	Gauss	Gauss–Lobatto
0.01	6.32	6.02	5.89	5.83	5.95	5.71	6.64
0.001	7.89	7.54	7.37	7.37	7.46	7.16	8.29
0.0001	9.75	9.29	9.12	9.12	9.21	8.88	10.19
0.00001	11.96	11.41	11.22	11.22	11.29	10.92	12.49

TABLE 6.4
 $PPW_{\min}(\delta)$ for the DGSEM with $N = 10$ and different optimized modal coefficients σ_N^{opt} and the DRP-like optimized variant with $\sigma_N^{DRP}(K_{\max}^* = 1.1) = 0.8127$. For comparison, the Gauss ($\sigma_N = 1$) DGSEM and the Gauss–Lobatto ($\sigma_N = 0.4762$) DGSEM with $N = 10$ are listed as well. Note that the optimization is with respect to dispersion; see Table 4.4 for comparison.

$\delta \backslash \sigma_N^{opt}$	0.5286	0.5322	0.7221	0.7995	DRP	Gauss	Gauss–Lobatto
0.01	4.92	4.92	4.76	4.70	4.69	4.56	4.98
0.001	5.66	5.64	5.47	5.41	5.40	5.27	5.71
0.0001	6.42	6.40	6.22	6.15	6.15	6.00	6.49
0.00001	7.24	7.24	7.04	6.96	6.94	6.80	7.32

yields the damping constant $\sigma_N = 1$, i.e., the Gauss DGSEM, as this means no additional filtering at all. However, we can investigate the dissipation behavior of the dispersion optimized schemes presented in section 4. We list the points per wavelength needed for a given dissipation accuracy in Tables 6.3 and 6.4 for polynomial degree $N = 5$ and $N = 10$, respectively, where we choose the modal filter constants σ_N according to the different dispersion optimization processes. For comparison purposes, the results of the Gauss and the Gauss–Lobatto scheme are listed as well. It is clear that the Gauss DGSEM is the most accurate one; it needs the lowest number of points per wavelength for a given accuracy requirement.

It is interesting to note that the dissipation relation plots, Figures 6.1(a) and 6.2(a), show that the dissipation error of the Gauss scheme is much higher compared to the Gauss–Lobatto scheme at coarse resolution, i.e., high wavenumbers K^* . This means that extremely coarsely resolved waves get much higher damping in the Gauss schemes, which points to a stability (robustness) advantage of the Gauss scheme in the case of underresolution. While this may not be of great importance for linear wave propagation, underresolution when discretizing nonlinear problems is of fundamental importance. The investigation of the stability behavior of both discretizations for nonlinear wave propagation problems is an actual topic of research. First investigations indeed point towards a stability advantage of the Gauss scheme for nonlinear problems in the case of coarse resolution computations [16, 6].

7. Conclusion. In this work, the dispersion and dissipation properties of Gauss and Gauss–Lobatto collocation discontinuous Galerkin discretizations for linear wave propagation is investigated. We show that the effect of underintegration (mass lumping) when Gauss–Lobatto points are used can be interpreted as the application of a modal filter where the highest mode is damped by the factor $\sigma_N = \frac{N}{2N+1}$. The effect of this modal filter, i.e., the Gauss–Lobatto underintegration, on the wave propagation properties is glaring. As a result, the Gauss DGSEM variant typically needs fewer points per wavelength for a given accuracy requirement and thus seems to be the right choice at first glance. Using the mechanism of modal filtering and its effect on the dispersion-dissipation relation, we can search for the optimal modal filter constant for a given dispersion error in the spirit of dispersion relation preserving FD schemes. This optimization process yields reasonable constants in highly competitive discretizations. Although it is debatable whether the results of such one-dimensional dispersion optimized schemes are applicable to general problems, it shows that modal filtering can be used to tune the dispersion relation with even better results than the Gauss DGSEM.

The dissipation analysis reveals that the Gauss variant, although much less dissipative for well-resolved scales, has much higher dissipation for large wavenumbers K compared to the Gauss–Lobatto scheme. This points towards an increased stability (robustness) of the Gauss DGSEM when a simulation is underresolved, which is supported by preliminary computational investigations. The robustness aspect of both variants is an ongoing topic of research and will be reported in future work.

The high accuracy of the Gauss DGSEM compared to the Gauss–Lobatto DGSEM comes at a price; namely, the stiffness of the Gauss discretization is much higher than the stiffness of the Gauss–Lobatto discretization. This directly translates into a time step advantage of the Gauss–Lobatto DGSEM. We showed that this factor depends on the boundary condition and that the safest estimate is to use the stability results with periodic boundary conditions. In the periodic case, the advantage of the Gauss–Lobatto scheme time step is about a factor of two. Thus, although the spatial accuracy of the Gauss variant is better, the reduced stiffness of the Gauss–Lobatto scheme could turn it into the more efficient scheme depending on the actual problem, i.e., on the spatial accuracy requirement and on the temporal accuracy requirements.

Appendix A. Dispersion relation for finite difference schemes. In this section the FD coefficients and the corresponding dispersion relation are listed for various schemes. We note that in the FD framework it is possible to derive exact analytical dispersion relation functions.

A.1. Central explicit O6 FD scheme. The coefficients read as

$$(A.1) \quad f'_j \approx \frac{1}{60} (-f_{j-3} + 9f_{j-2} - 45f_{j-1} + 45f_{j+1} - 9f_{j+2} + f_{j+3}).$$

The dispersion function is

$$(A.2) \quad \operatorname{Re}(\Omega(K)) = \frac{1}{30} \sin(3K) - \frac{3}{10} \sin(2K) + \frac{3}{2} \sin(K).$$

A.2. One cell biased explicit O6 FD scheme. The coefficients read as

$$(A.3) \quad f'_j \approx \frac{1}{60} (2f_{j-2} - 24f_{j-1} - 35f_j + 80f_{j+1} - 30f_{j+2} + 8f_{j+3} - f_{j+4}).$$

The dispersion function is

$$(A.4) \quad \operatorname{Re}(\Omega(K)) = -\frac{8}{15} \sin(2K) + \frac{26}{15} \sin(K) + \frac{2}{15} \sin(3K) - \frac{1}{60} \sin(4K).$$

A.3. Two cell biased explicit O6 FD scheme. The coefficients read as

$$(A.5) \quad f'_j \approx \frac{1}{60} (-10f_{j-1} - 77f_j + 150f_{j+1} - 100f_{j+2} + 50f_{j+3} - 15f_{j+4} + 2f_{j+5}).$$

The dispersion function is

$$(A.6) \quad \operatorname{Re}(\Omega(K)) = \frac{8}{3} \sin(K) - \frac{5}{3} \sin(2K) + \frac{5}{6} \sin(3K) - \frac{1}{4} \sin(4K) + \frac{1}{30} \sin(5K).$$

A.4. Central compact O6 FD scheme. The coefficients read as

$$(A.7) \quad f'_{j-1} + 3f'_j + f'_{j+1} \approx \frac{1}{12} (-f_{j-2} - 28f_{j-1} + 28f_{j+1} + f_{j+2}).$$

The dispersion functions result to

$$(A.8) \quad \operatorname{Re}(\Omega(K)) = \frac{\frac{1}{6} \sin(2K) + \frac{14}{3} \sin(K)}{2 \cos(K) + 3}.$$

Acknowledgment. The authors would like to thank Andreas Babucke for providing the Maple worksheets for the finite difference dispersion analysis.

REFERENCES

- [1] M. AINSWORTH AND H. A. WAJID, *Dispersive and dissipative behavior of the spectral element method*, SIAM J. Numer. Anal., 47 (2009), pp. 3910–3937.
- [2] M. AINSWORTH, *Dispersive and dissipative behaviour of high order discontinuous Galerkin finite element methods*, J. Comput. Phys., 198 (2004), pp. 106–130.
- [3] A. BABUCKE, *Direct Numerical Simulation of Noise-Generation Mechanisms in the Mixing Layer of a Jet*, Dissertation, University of Stuttgart, Stuttgart, Germany, 2009.
- [4] K. BLACK, *A conservative spectral element method for the approximation of compressible fluid flow*, Kybernetika, 35 (1999), pp. 133–146.
- [5] K. BLACK, *Spectral element approximation of convection-diffusion type problems*, Appl. Numer. Math., 33 (2000), pp. 373–379.
- [6] N. CASTEL, G. COHEN, AND M. DURUFLE, *Application of discontinuous Galerkin spectral method on hexahedral elements for aeroacoustic*, J. Comput. Acoust., 17 (2009), pp. 175–196.
- [7] S. DENG, W. CAI, AND V. ASTRATOV, *Numerical study of light propagation via whispering gallery modes in microcylinder coupled resonator optical waveguides*, Optics Express, 12 (2004), pp. 6468–6480.
- [8] S. DENG, *Numerical simulation of optical coupling and light propagation in coupled optical resonators with size disorder*, Appl. Numer. Math., 57 (2007), pp. 475–485.
- [9] S. FAGHERAZZI, D. FURBISH, P. RASSETARINERA, AND M. Y. HUSSAINI, *Application of the discontinuous spectral Galerkin method to groundwater flow*, Adv. Water Res., 27 (2004), pp. 129–140.
- [10] S. FAGHERAZZI, P. RASSETARINERA, M. Y. HUSSAINI, AND D. J. FURBISH, *Numerical solution of the dam-break problem with a discontinuous Galerkin method*, J. Hydraulic Engrg., 130 (2004), pp. 532–539.
- [11] F. GIRALDO, J. HESTHAVEN, AND T. WARBURTON, *Nodal high-order discontinuous Galerkin methods for the spherical shallow water equations*, J. Comput. Phys., 181 (2002), pp. 499–525.

- [12] F. GIRALDO AND M. RESTELLI, *A study of spectral element and discontinuous Galerkin methods for the Navier–Stokes equations in nonhydrostatic mesoscale atmospheric modeling: Equation sets and test cases*, J. Comput. Phys., 227 (2008), pp. 3849–3877.
- [13] J. HESTHAVEN AND T. WARBURTON, *Nodal Discontinuous Galerkin Methods: Algorithms, Analysis, and Applications*, Springer-Verlag, New York, 2008.
- [14] F. HU, M. HUSSAINI, AND P. RASSETARINERA, *An analysis of the discontinuous Galerkin method for wave propagation problems*, J. Comput. Phys., 151 (1999), pp. 921–946.
- [15] D. A. KOPRIVA, *Implementing Spectral Methods for Partial Differential Equations: Algorithms for Scientists and Engineers*, Springer-Verlag, Berlin, 2009.
- [16] D. KOPRIVA AND G. GASSNER, *On the quadrature and weak form choices in collocation type discontinuous Galerkin spectral element methods*, J. Sci. Comput., 44 (2010), pp. 136–155.
- [17] D. KOPRIVA, S. WOODRUFF, AND M. HUSSAINI, *Discontinuous spectral element approximation of Maxwell’s equations*, in Proceedings of the International Symposium on Discontinuous Galerkin Methods, B. Cockburn, G. Karniadakis, and C.-W. Shu, eds., Lect. Notes Comput. Sci. Eng. 11, Springer-Verlag, Berlin, 2000, pp. 355–361.
- [18] D. KOPRIVA, S. WOODRUFF, AND M. HUSSAINI, *Computation of electromagnetic scattering with a non-conforming discontinuous spectral element method*, Internat. J. Numer. Methods Engrg., 53 (2002), pp. 105–122.
- [19] F. LÖRCHER, G. GASSNER, AND C.-D. MUNZ, *Arbitrary high order accurate time integration schemes for linear problems*, in Proceedings of the European Conference on Computational Fluid Dynamics, 2006.
- [20] P. RASSETARINERA AND M. HUSSAINI, *An efficient implicit discontinuous spectral Galerkin method*, J. Comput. Phys., 172 (2001), pp. 718–738.
- [21] P. RASSETARINERA, D. KOPRIVA, AND M. HUSSAINI, *Discontinuous spectral element solution of acoustic radiation from thin airfoils*, AIAA J., 39 (2001), pp. 2070–2075.
- [22] M. RESTELLI AND F. X. GIRALDO, *A conservative discontinuous Galerkin semi-implicit formulation for the Navier–Stokes equations in nonhydrostatic mesoscale modeling*, SIAM J. Sci. Comput., 31 (2009), pp. 2231–2257.
- [23] S. SHERWIN, *Dispersion analysis of the continuous and discontinuous Galerkin formulations*, in Proceedings of the International Symposium on Discontinuous Galerkin Methods, Springer-Verlag, Berlin, 1999, pp. 425–431.
- [24] D. STANESCU, F. FARASSAT, AND M. HUSSAINI, *Aircraft Engine Noise Scattering—Parallel Discontinuous Galerkin Spectral Element Method*, Technical report 2002-0800, AIAA, 2002.
- [25] D. STANESCU, D. KOPRIVA, AND M. HUSSAINI, *Dispersion analysis for discontinuous spectral element methods*, J. Sci. Comput., 15 (2001), pp. 149–171.
- [26] D. STANESCU, J. XU, F. FARASSAT, AND M. HUSSAINI, *Computation of engine noise propagation and scattering off an aircraft*, Aeroacoustics, 1 (2002), pp. 403–420.
- [27] C. TAM AND H. SHEN, *Direct Computation of Nonlinear Acoustic Pulses using High-Order Finite Difference Schemes*, Technical report 93-4325, AIAA, 1993.
- [28] E. TORO, *Riemann Solvers and Numerical Methods for Fluid Dynamics*, 2nd ed., Springer-Verlag, Berlin, 1999.